

**On-surface synthesis of chevron-like graphene  
nanoribbons from a molecular precursor**  
characterization with STM and STS

*Author*

Koen Houtsma

*First examiner*

prof. dr. M.A. Stöhr

*Second examiner*

prof. dr. T. Banerjee

*Daily supervisor*

dr. M. Enache

12th of April, 2019



**university of  
groningen**

**faculty of science  
and engineering**

## Abstract

Graphene is an exciting material with excellent electronic properties, however it lacks a band gap which makes it unsuitable for application in field effect devices. By cutting the graphene into narrow strips, a band gap may be opened. Recently the possibility to create graphene nanoribbons (GNRs) with atomic precision using surface-assisted coupling has emerged. This has allowed for many interesting new possibilities, such as control over the edge termination and ribbon width. In this thesis, starting with the prochiral 6,12,-dibromochrysene as a molecular precursor, we fabricated GNRs with a distinctive chevron-like shape. The structural and electronic properties of these GNRs were investigated. Using scanning tunneling spectroscopy, we measured its band gap to be  $1.3 \pm 0.1$  eV. In addition, differential conductance maps reveal edge states in these ribbons. Based on comparison of both experimental results and *ab initio* calculations, it seems likely that the chevron-like GNR has a wider band gap than an armchair-edge GNR of the same width. This opens up a possibility to tune the band gap of GNRs not only by changing its width or edge termination, but by changing its overall shape.

# Contents

<b>1</b>	<b>Introduction</b>	<b>4</b>
<b>2</b>	<b>Theory</b>	<b>6</b>
2.1	Molecular self-assembly on surfaces . . . . .	6
2.1.1	Energy balance for self-assembly . . . . .	6
2.1.2	Intermolecular interactions . . . . .	7
2.1.2.1	Hydrogen bonding . . . . .	7
2.1.2.2	Halogen bonding . . . . .	7
2.1.2.3	Van der Waals interaction . . . . .	8
2.2	On-surface synthesis . . . . .	9
2.2.1	Ullmann coupling . . . . .	9
2.2.2	Cyclodehydrogenation . . . . .	10
2.3	Graphene and its properties . . . . .	10
2.3.1	Graphene . . . . .	11
2.3.2	Graphene nanoribbons . . . . .	12
<b>3</b>	<b>Experimental methods</b>	<b>15</b>
3.1	Scanning tunneling microscopy . . . . .	15
3.1.1	The quantum tunneling phenomenon . . . . .	15
3.1.2	Tunneling in an STM . . . . .	16
3.1.2.1	Bardeen's formalism . . . . .	17
3.1.2.2	The s-wave tip model . . . . .	18
3.1.3	Operation principle of an STM . . . . .	20
3.2	Scanning tunneling spectroscopy . . . . .	20
3.3	The experimental setup . . . . .	21
3.4	Sample cleaning and preparation . . . . .	23
<b>4</b>	<b>Results</b>	<b>25</b>
4.1	Self-assembled networks formed by DBCh on Au(111) . . . . .	25
4.2	Chevron-like graphene nanoribbons from DBCh . . . . .	26
<b>5</b>	<b>Discussion</b>	<b>35</b>

<b>6</b>	<b>Conclusion</b>	<b>36</b>
<b>7</b>	<b>Acknowledgements</b>	<b>43</b>

# 1 Introduction

When the first personal computers hit the market in 1977, the number of transistors in their integrated circuits (ICs) was of the order of magnitude  $10^3$ . Now, it is commonplace to have  $10^9$  transistors in the ICs for a mobile phone, a device that fits in a pocket. The transistor count in ICs empirically follows an exponential growth termed Moore's Law (after Gordon Moore, the co-founder of Intel, who observed this trend in 1965 and predicted for it to continue [1]). The demand for devices that are small and cheap, yet fast requires ingenuity in the creation of new IC manufacturing processes. As of now, the most common way to mass produce ICs is photolithography, where light is used to create a pattern on a silicone wafer. Using photolithography, it is now possible to manufacture ICs with feature sizes as small as 7 nanometer. However, the rapid increase in transistor count as predicted by Moore's Law is slowing, and so new solutions for the manufacturing of ICs have to be found in order to keep up with the technological demand

Nanoscience is the study of structures that have a characteristic length scale of 1 to 100 nanometer, which coincides for the length scale required for smaller ICs. The processes used to create structures at these length scales can be divided into two categories, the top-down and bottom-up approaches. The top-down approach (e.g. photolithography) starts with a bulk sized material and by cutting, shaping and etching, it is transformed into a nanometer-sized object. On the other hand, the bottom-up approach starts from atoms and molecules and works its way up from there. Using a bottom-up approach, it is now possible to fabricate nanometer-sized architectures with atomic precision [2] and therefore this approach is a promising candidate for a new generation of devices.

Of particular interest for this study and nanoscience in general is graphene. Graphene is a two-dimensional sheet of carbon atoms arranged in a honeycomb lattice. The discovery of the field effect in graphene [3] coupled with its high charge carrier mobility [4] has sparked an enormous interest in graphene and graphene-based devices. However, in graphene the valence and conduction band come together in the Dirac point and thus, graphene

is a zero gap semimetal. As a result, graphene does not have an 'off' state at room temperature when implemented in devices. Therefore, for using graphene in a next generation of electronic devices, its properties have to be tuned.

To open a band gap (and thus allowing for a true 'off' state) in graphene a number of strategies can be employed, such as changing its shape or doping. For this thesis, the first option is of particular interest. By cutting the graphene sheet into narrow ribbons (graphene nanoribbons, GNRs), quantum confinement takes place and a band gap can be opened. Because the exact electronic properties of GNRs also depend on their edge termination [5] it is of interest to create GNRs with atomic precision. This brings us back to the two strategies of production: top-down and bottom-up. The top-down methods have thus far been unable to control the exact edge termination because of their limited precision [6]. Contrastingly, using on-surface synthesis, a bottom-up approach, creating GNRs with atomic precision is possible and even common. On-surface synthesis starts with molecular precursors which, mediated by the surface, form polymers upon heating. This process relies both on molecule-molecule and molecule-surface interactions to form intricate molecular networks, chains or other structures. In this way, GNRs with armchair [7–9], zigzag [10] and chiral [11, 12] edge terminations have been created, as well as GNRs with chevron-like topology [13, 14] and various GNR heterostructures [15–20].

Using a scanning tunneling microscope (STM), it is possible to take real space images with high resolution (up to a single atom [21]) of GNRs and their molecular precursors to study their structure. Using a related technique, scanning tunneling spectroscopy (STS), the electronic properties of GNRs can be probed. In this thesis, GNRs with chevron topology will be created on the Au(111) surface according to Pham *et al.* [13]. Both the structural and electronic properties of the nanoribbons will be characterized using STM and STS, respectively. To better understand these techniques, a brief introduction will be given in section 3, where the sample preparation will also be discussed. The theoretical background will be discussed in section 2.

## 2 Theory

### 2.1 Molecular self-assembly on surfaces

Supramolecular chemistry is the study of chemistry 'beyond the molecule' [22]. It describes how systems of molecules interact to create higher order assemblies [23]. For this thesis, an important part of supramolecular chemistry is the self-assembly of molecules to form molecular networks. Molecular self-assembly was described by Whitesides in 1991 as "the spontaneous association of molecules under equilibrium conditions into stable, structurally well-defined aggregates joined by noncovalent bonds." [24]. Molecular self-assembly can take place both in solution (see for instance [25]) and on-surface. However, in this section only molecular self-assembly on surfaces will be considered. Some examples of molecular self-assembly on surfaces include the assembly of clusters [26], chains [26] and porous networks [13, 27].

Here, we will briefly discuss the delicate energy balance required for self-assembly and a few molecular interactions common in self-assembled networks.

#### 2.1.1 Energy balance for self-assembly

For molecular self-assembly to take place, a number of requirements for the different energies at play have to be met. Once molecules have been deposited on a substrate, the energies that play an important role are the binding energy to the substrate ( $E_b$ ), the molecule-molecule interaction energy ( $E_{\text{inter}}$ ), the kinetic energy of the molecules on the surface ( $E_{\text{kin}}$ ) and the energy required for the molecules to diffuse over the surface ( $E_d$ ). Here, we will briefly discuss how these different factors affect the process of molecular self-assembly according to Kühnle [28].

Naturally, once molecules are adsorbed on the surface, they should be able to diffuse over the surface in order to come into contact with other molecules and to self-assemble. Therefore, the kinetic energy the molecules have should be above the diffusion barrier. However, if the kinetic energy of the molecules becomes larger than the molecule-molecule interaction

energy, no self-assembly will take place either. Of course, the kinetic energy of the molecules on the surface should not exceed the binding energy of the molecules to the substrate, otherwise the molecules would simply desorb. In summary:

$$E_b \geq E_{\text{kin}} > E_d, \quad (1)$$

$$E_{\text{inter}} \geq E_{\text{kin}} > E_d. \quad (2)$$

For a more detailed description of the different energies and their roles, as well as discussions on the role of molecular flux and adsorption strength (physisorption and chemisorption), we refer to Kühnle’s review paper [28]. In general, the exact structure formed depends on an interplay of both molecule-molecule and molecule-substrate interactions as well as molecular coverage, among others.

## 2.1.2 Intermolecular interactions

### 2.1.2.1 Hydrogen bonding

Hydrogen bonding can occur when a hydrogen atom in a molecule is bonded to a group more electronegative than itself (commonly oxygen or nitrogen). The more electronegative group pulls on the electron of the hydrogen atom, making it slightly positively charged. The simplest example of this is the water molecule,  $\text{H}_2\text{O}$ , where the oxygen pulls on the electron of the hydrogen atom. The slightly positive hydrogen will feel a net attractive force to regions of molecules that are negatively charged. In the example of pure water the negatively charged regions would be the oxygen atoms. This interaction, where the partially positive hydrogen interacts with negative molecular sites is known as hydrogen bonding. A few examples of hydrogen bonding in self-assembly include porous networks [27–29], ribbons [30] and close-packed structures [28, 31].

### 2.1.2.2 Halogen bonding

If a compound of the form  $\text{R-X}$ , with  $\text{X}$  a halogen and  $\text{R}$  a group covalently bound to that halogen, is formed, a non-covalent attractive interaction can occur between the bonded halogen and a negative molecular site. This

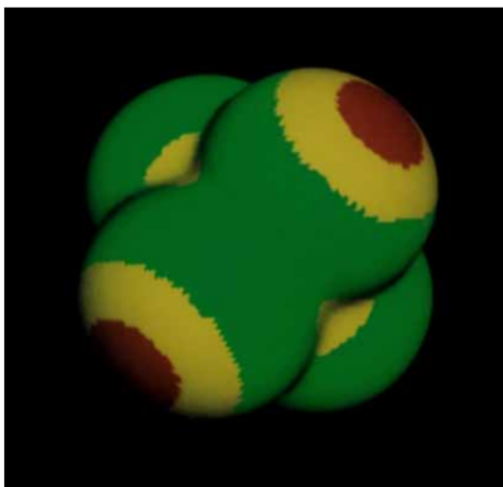


**Figure 1:** The calculated electrostatic potential  $V(r)$  of  $\text{CBr}_4$ . Colour map for  $V(r)$  in kcal/mol: red for  $V(r) > 14$ , yellow for  $0 < V(r) < 14$ , green for  $-14 < V(r) < 0$ . The red and yellow areas together form the  $\sigma$ -hole. Source: [33]

is called halogen bonding [32]. From this perspective, halogen bonding is quite similar to hydrogen bonding described in the previous section. The possibility of the halogen bond is due to a feature known as the  $\sigma$ -hole, found by Brinck *et al.* in 1992 [33]. Brinck *et al.* calculated the electrostatic potentials of bonded halogens (see figure 1) and found that although the halogen has an overwhelmingly negative electrostatic potential (green in the figure), there is an area of positive electrostatic potential on the R-X bond axis known as the  $\sigma$ -hole (red and yellow in the figure). The halogen bond has some advantages over the hydrogen bond. Because the  $\sigma$ -hole is confined to a relatively small area, the bonds take place mostly in a 'head-on' manner. Because the slight positive charge of hydrogen bond donors is more uniformly distributed, the range of angles in which the interaction can take place is much wider. Therefore, the halogen bond allows for a more directional bonding than hydrogen bonding. In addition, the strength of the halogen bond can be tuned in a facile manner by substitution of a different halogen (heavier halogens form weaker halogen bonds) [34].

### 2.1.2.3 Van der Waals interaction

Van der Waals interactions describe a set of weak, non-covalent interactions between molecules. They can be divided into three groups. The first

is the Keesom force (or dipole-dipole force) where two dipolar molecules interact attractively or repulsively. The second is the Debye force (or dipole-induced-dipole force) where one dipolar molecule induces a dipole in another (non-polar) molecule causing the two molecules to interact attractively. The last force, felt by all molecules, is the London dispersion force (or simply dispersion force). Every molecule has an instantaneous fluctuating dipole moment. When two molecules are brought together, the one with the stronger fluctuating dipole moment induces an opposite fluctuating dipole moment in the other resulting in an attractive force [35]. The London dispersion force is weaker than halogen- and hydrogen bonding and non-directional. Some examples of self-assembly through Van der Waals interactions include porous and linear networks [36, 37].

## 2.2 On-surface synthesis

The surface plays an important role for the synthesis of various molecular structures. It can guide the molecular growth along a certain substrate direction [38, 39] or act as the catalyst for a reaction as is the case for Ullmann coupling. Here we will briefly discuss two important, surface-assisted, reactions: Ullmann coupling and cyclodehydrogenation.

### 2.2.1 Ullmann coupling

Ullmann coupling, after Fritz Ullmann who discovered it in 1901 [40], is a reaction where two aryl halides couple to form a biaryl, mediated by a copper catalyst [41]. Ullmann coupling has proven to be a useful and versatile tool for the design of on-surface nanostructures and is used commonly [42]. A good example of the usefulness of Ullmann coupling in the design of on-surface nanostructures is the publication by Grill *et al.* [43], where depending on the number and location of bromine substituents one-dimensional chains or two-dimensional networks were formed after a thermal activation step. For the case of on-surface synthesis of GNRs, it is common to observe a polymer intermediate formed through Ullmann-type coupling, see for instance [2, 8, 13, 44].

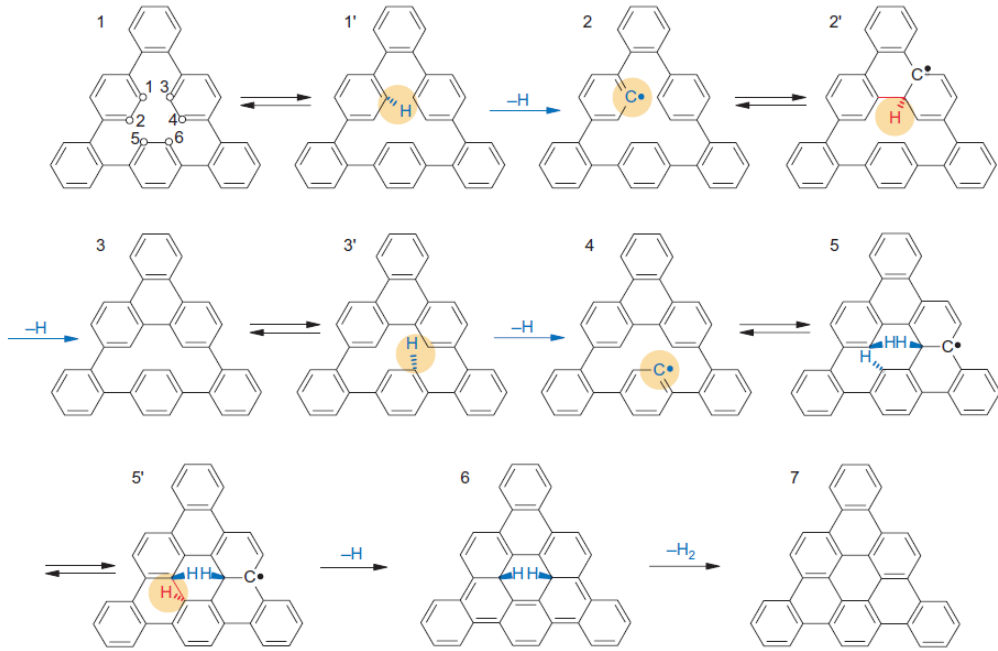


**Figure 2:** The reaction path from a polyphenylene (**1**) to a nanographene (**7**) on Cu(111) through five metastable intermediate states (**2-6**). The primed numbers indicate a specific conformation of the molecules during the reaction step. The yellow circles indicate that the copper substrate is catalytically active. The reaction path shown here is supported by a combination of STM measurements and *ab initio* density functional theory (DFT) calculations. Adapted from [45]

### 2.2.2 Cyclodehydrogenation

The polymer intermediates formed after Ullmann-type coupling are, in the case of creating GNRs, comprised of multiple coupled phenyl rings. Upon further thermal annealing, a surface assisted intramolecular coupling of phenyl rings can take place [45]. This coupling is known as cyclodehydrogenation. Figure 2 shows a step-by-step transformation from a polyphenylene to a nanographene on a Cu(111) substrate. The yellow circles indicate reaction steps where the copper substrate atoms are catalytically active.

## 2.3 Graphene and its properties

In this section, we will give a brief description of graphene and its electronic properties. We will start with a description on the basis of the work

of Castro Neto *et al.* [46]. Subsequently, we will discuss the effects of reducing the dimensionality of the two-dimensional graphene sheet into a one-dimensional strip.

### 2.3.1 Graphene

Graphene is a flat sheet of  $sp^2$  hybridized carbon in a honeycomb lattice. The two lattice vectors of the structure are given by:

$$\vec{a}_1 = \frac{a}{2}(3, \sqrt{3}), \quad \vec{a}_2 = \frac{a}{2}(3, -\sqrt{3}) \quad (3)$$

with  $a \approx 1.42 \text{ \AA}$  [46]. From this, the reciprocal lattice vectors can be obtained using the usual methods. Each lattice point has two carbon atoms associated with it, one on the lattice point and one shifted by  $a(1,0)$ . The crystal thus has two sublattices, A and B. In this crystal, each carbon has three nearest neighbours. In figure 3a the lattice vectors  $\vec{a}_i$  and nearest neighbour vectors  $\vec{\delta}_i$  are depicted. By considering the  $p_z$  orbitals of the carbon atoms, it is now possible to solve for the electronic dispersion relationship of the  $\pi$ -electrons in the context of a tight-binding model. However, here we will simply state the result. Already in 1947, long before the experimental realization of graphene, Wallace found the dispersion relation:

$$E_{\pm}(\vec{k}) = \pm t\sqrt{3 + f(\vec{k})} - t'f(\vec{k}) \quad (4)$$

with  $t, t'$  the nearest and next-nearest neighbour hopping energy and

$$f(\vec{k}) = 2 \cos(\sqrt{3}k_y a) + 4 \cos\left(\frac{\sqrt{3}}{2}k_y a\right) \cos\left(\frac{3}{2}k_x a\right). \quad (5)$$

Equations (4) and (5) give the entire dispersion relationship of the  $\pi$  electrons. The electronic dispersion is given in figure 3b. The plus sign in equation (4) corresponds to the upper band, whereas the minus sign corresponds to the lower band. Of special interest to the electronic properties of graphene are the states close to the Fermi level. These states sit close to the two Dirac points (also known as the  $\mathbf{K}$  and  $\mathbf{K}'$  points). Wallace showed that when the dispersion relation is expanded (neglecting next-nearest neighbour hopping) close to one of these Dirac points we obtain:

$$E_{\pm} = \pm v_F |\vec{q}| \quad (6)$$

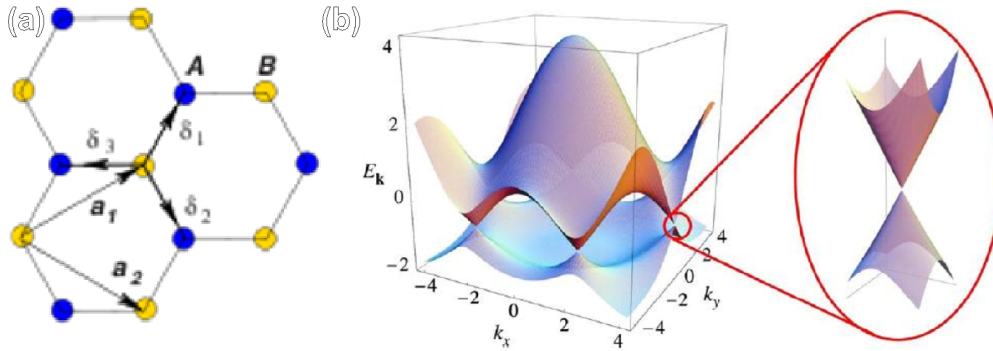


**Figure 3:** a) Schematic model of the graphene honeycomb lattice with the two unit cell vectors  $\vec{a}_1, \vec{a}_2$  and the three nearest neighbour vectors  $\vec{\delta}_1, \vec{\delta}_2, \vec{\delta}_3$  indicated. The A sublattice points are colored in blue while the B sublattice points are colored in yellow. b) The band structure of graphene's  $\pi$ -electrons obtained from a tight binding model with nearest neighbour hopping  $t = 2.7$  eV and next-nearest neighbour hopping  $t' = 0.2t$ . A close-up of one Dirac point is shown, which reveals the linear dispersion Dirac cones. Source: [46]

with  $\vec{q} = \vec{k} - \mathbf{K}$ , the momentum measured with  $\mathbf{K}$  as the origin and  $v_F = 3at/2$  the Fermi velocity. Interestingly, the electronic dispersion relation described by equation (6) is linear, strikingly different from the usual parabolic dispersion found in everyday metals. The linear dispersion around the Dirac point forms two cones known as the Dirac cones. These Dirac cones, among others, are responsible for some of graphene's outstanding electronic properties. It is interesting to note that the electrons in graphene can be described by the relativistic Dirac equation, where  $v_F$  takes on the role of the speed of light [46, 47].

The emergence of the Dirac cones from the tight-binding model concludes our discussion of bulk graphene. For a more in depth treatment, we refer to the excellent review by Castro Neto *et al.* [46].

### 2.3.2 Graphene nanoribbons

The simplest graphene nanoribbons are those with a pure armchair or zigzag edge termination, called AGNRs and ZGNRs, respectively. The act of 'cutting' the graphene in a narrow strip means that the electrons will be confined in one direction. When an infinite potential outside the GNR is assumed, it is easy to see that this confinement leads to discrete

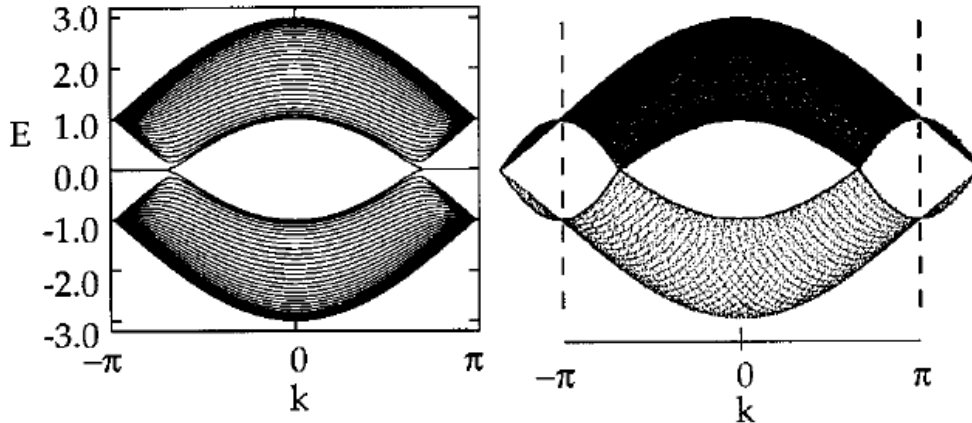


**Figure 4:** The band structure of a  $N=30$  wide ZGNR using (left) tight binding calculations and (right) the zone folding technique as discussed in the text. A flatband feature at  $|k| > 2/3\pi$  is observed in the calculated band structure that is not seen in the zone folding band structure. Source: [48]

allowed values for  $k$  in the confined direction. A facile manner to approximate the behaviour of GNRs is the zone-folding technique as presented in the work of Nakada *et al.* [48]. To approximate the band structure of GNRs, slices of the bulk graphene electronic dispersion are taken at the allowed  $k$  values. This technique predicts that for AGNRs, only the ones with  $N = 3p + 2$  (with  $p$  an integer) carbon atoms in the transverse direction are semimetallic, whereas the others have a band gap. It predicts that zigzag GNRs are always semimetallic, having a Dirac point at  $k = \pm 2/3\pi$  [48]. However, when calculating the band structure of ZGNRs using the tight binding method (figure 4, right) an interesting flatband feature is observed in the calculated band structure that is not seen in the zone-folding band structure (figure 4, left). This state originates at the zigzag edge and decays exponentially into the ribbon [48].

Moreover, *ab initio* density functional theory (DFT) calculations show that AGNRs can be divided into three distinct classes<sup>1</sup>: the  $3p$ ,  $3p + 1$  and  $3p + 2$  class. The band gap versus the ribbon width is given for both tight binding and DFT calculations in figure 5a and b respectively. The AGNRs can thus be divided in small ( $3p + 2$ ), medium ( $3p$ ) and large band gap

<sup>1</sup>Rather than the two identified earlier

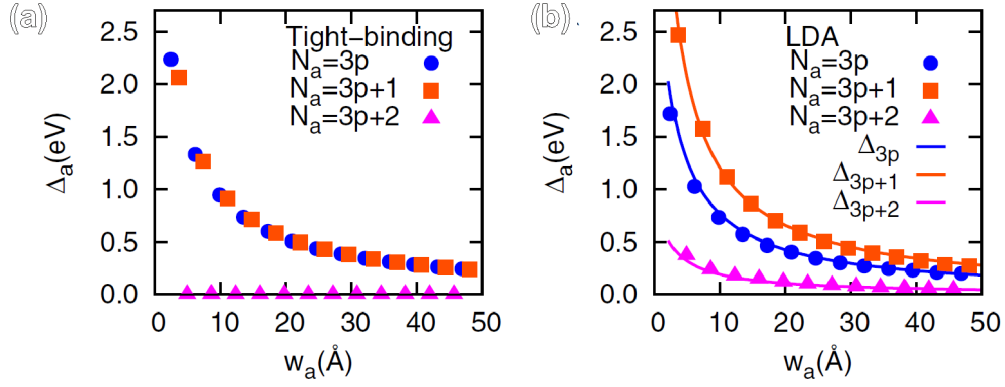


**Figure 5:** The calculated band gap for AGNRs of various widths. a) Tight binding calculations showing two groups: semiconducting and semimetallic ones. b) DFT calculations showing three groups: small ( $3p+2$ ), medium ( $3p$ ) and large band gap ( $3p+1$ ) ones. Source: [49]

( $3p+1$ ) ribbons. Because of this, a decrease in width does not always lead to an increase in band gap. Otherwise, however, the band gap of AGNRs goes approximately inversely with the width.

## 3 Experimental methods

### 3.1 Scanning tunneling microscopy

The STM, invented by Binnig and Rohrer in 1981, is a device where an atomically sharp metallic tip is brought close (a few Ångströms distance) to a conducting sample surface [50]. When a bias is applied between tip and sample, a directional tunneling current will flow. By scanning the tip over the surface an image of the topology<sup>2</sup> of the surface is acquired.

To interpret measurement data of any kind, it is important to understand how the measurement device works. To this end, the working principle of an STM will be discussed briefly.

#### 3.1.1 The quantum tunneling phenomenon

To better understand the working of an STM, it is illustrative to first discuss an elementary model for quantum tunneling. We consider the case with three regions: **I** and **III** with potential  $U = 0$ , separated by region **II** with potential  $U = U_0$ , see figure 6. For the description of quantum tunneling, we will assume the electrons come from region **I** and tunnel through region **II** into region **III**. In a quantum mechanics, electrons are described by the time-independent Schrödinger equation:

$$\left(-\frac{\hbar^2}{2m}\frac{d^2}{dz^2} + U(z)\right)\Psi(z) = E\Psi(z), \quad (7)$$

where  $\hbar$  is the reduced Planck's constant,  $m$  is the electron mass,  $U(z)$  is the potential,  $\Psi(z)$  is the electron's wavefunction and  $E$  is the electron's energy. The term within brackets is the Hamiltonian operator (in one dimension). Note that the Schrödinger equation is an eigenvalue problem, where  $\Psi(z)$  and  $E$  represents the eigenfunctions and eigenvalues of the Hamiltonian operator, respectively. The solution of this eigenvalue problem in the two classically allowed regions are:

$$\Psi_{\text{I}}(z) = A \exp(ikz) + B \exp(-ikz) \quad (8)$$

---

<sup>2</sup>What an STM actually measures, as will become apparent shortly, is slightly more subtle.

$$\Psi_{\text{III}}(z) = F \exp(ikz) \quad (9)$$

with  $k = \sqrt{2mE}/\hbar$ . Equation (8) describes both a right traveling wave and a reflected, left traveling wave in region **I**. On the other hand, equation (9) only describes a right traveling wave in region **III**.  $A$ ,  $B$  and  $F$  are constants to be found using appropriate boundary conditions. In the classically forbidden region, equation (7) has the solution:

$$\Psi_{\text{II}}(z) = C \exp(\kappa z) + D \exp(-\kappa z) \quad (10)$$

where  $C$  and  $D$  constants and  $\kappa = \sqrt{2m(E - U_0)}/\hbar = i\sqrt{2m(U_0 - E)}/\hbar$ . By inspection of equation (7), we observe that a (non-trivial) solution for the wavefunction must be twice differentiable. Therefore, the wavefunction and its derivative have to be continuous. This yields the boundary conditions required to solve the problem. The exact solution for the probability of transmission [51]  $T = (F/A)^2$  is:

$$T = \frac{1}{1 + \frac{V_0^2 \sinh^2(\kappa a)}{4E(V_0 - E)}} \quad (11)$$

where  $a$  is the barrier width. By considering the limit where  $\kappa a \gg 0$  a simplified equation for the transmission probability can be obtained:

$$T \approx \frac{16E(U_0 - E)}{U_0^2} \exp(-2\kappa a). \quad (12)$$

From this equation it is clear that the tunneling probability decays exponentially and that the transmission probability is very sensitive to the barrier width.

### 3.1.2 Tunneling in an STM

Now we consider the theory of quantum tunneling through a potential barrier from section 3.1.1 as applied to an STM. The work function of a metal is defined as the minimum energy required to remove one electron from the bulk [52]. Thus, the work function takes on the role of  $E - U_0$  in the expression for  $\kappa$ . Now we apply a bias voltage  $-V$  between the sample and tip, which allows the states between  $E_F - eV$  and  $E_F$  to tunnel from

the sample to the tip, see figure 7. The probability of finding an electron in sample state  $\nu$  at the metal surface is  $|\Psi_\nu(0)|^2$  and thus the probability of finding the electron at the tip:

$$P \propto |\Psi_\nu(0)|^2 \exp(-2\kappa a) \quad (13)$$

where 0 was taken to be the position of the sample-vacuum interface and  $a$  is the tip-sample separation (which in the case of an STM takes on the role of the barrier width) [52]. By summing over all the states that are eligible to tunnel an expression for the current is derived:

$$I \propto \sum_{E=E_F-eV}^{E_F} |\Psi_\nu(0)|^2 \exp(-2\kappa a). \quad (14)$$

As a last step, we note that the sample local density of states (LDOS) is given by

$$\rho_S(z, E) = \frac{1}{eV} \sum_{E=E_F-eV}^{E_F} |\Psi_\nu(z)|^2 \quad (15)$$

and thus:

$$I \propto V \rho(0, E_F) \exp(-2\kappa a), \quad (16)$$

which gives a first model for the tunneling current of an STM [52]. From this expression it is clear that the tunneling current scales with both the bias voltage and density of states which intuitively makes sense. Also an inverse exponential scaling with distance is observed, which means that in practice the tip and sample have to be separated by not more than a few Ångströms of vacuum to function.

### 3.1.2.1 Bardeen's formalism

A more sophisticated solution for the tunneling current problem came from Bardeen in 1961. Bardeen gave a solution for the tunneling current between two electrodes separated by an insulating barrier using time-dependent perturbation theory [52, 54]. The current found at 0K using this approach is

$$I = \frac{4\pi e}{\hbar} \int_0^{eV} \rho_L(E_F - eV + \epsilon) \rho_R(E_F + \epsilon) |M|^2 d\epsilon \quad (17)$$

where  $V$  is the applied bias voltage between left and right electrode,  $M$  the matrix element for the transition from non-tunneled to tunneled state (i.e.

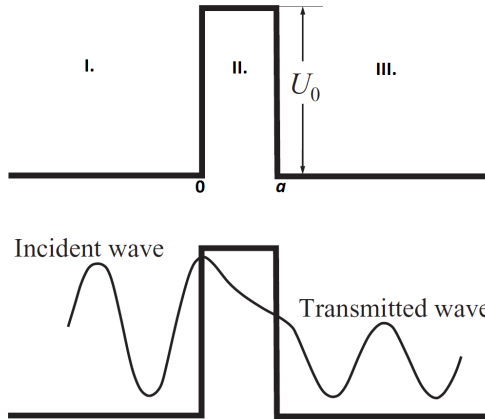


**Figure 6:** Tunneling through a classically forbidden barrier. The top image shows the relevant variables (barrier height and width), as well as the three regions discussed in the main text. The bottom image shows an incident wave in region **I**, which describes an right moving electron. When the electron impinges on the potential step it has a probability of entering into region **II**. In region **III** the transmitted wave is shown. Note that its amplitude is smaller than the incident wave, indicating that the probability of finding the electron beyond the barrier is smaller than finding the electron in region **I**. Adapted from [53]

the state where an electron has tunneled from the left to the right electrode) and  $\rho_L$  and  $\rho_R$  the DOS of left and right electrode, respectively. For temperatures above 0K, the occupation probability of the electron states has to be taken into account using the Fermi distribution. This theory can be applied to an STM by treating the sample as one electrode and treating the tip as the other.

### 3.1.2.2 The s-wave tip model

Comparison of measurements and theory came just after the invention of the STM. A model often used by the STM community is that of Tersoff and Hamann [55]. The apex of the tip is treated as a metallic sphere with radius of curvature  $r_0$  whereas the surface is treated exactly. The wavefunction of the tip is expanded in a series of spherical harmonics. Tersoff and Hamann only used the first spherical harmonic, the s-wave. This allows for an evaluation of the tunneling matrix element and subsequently

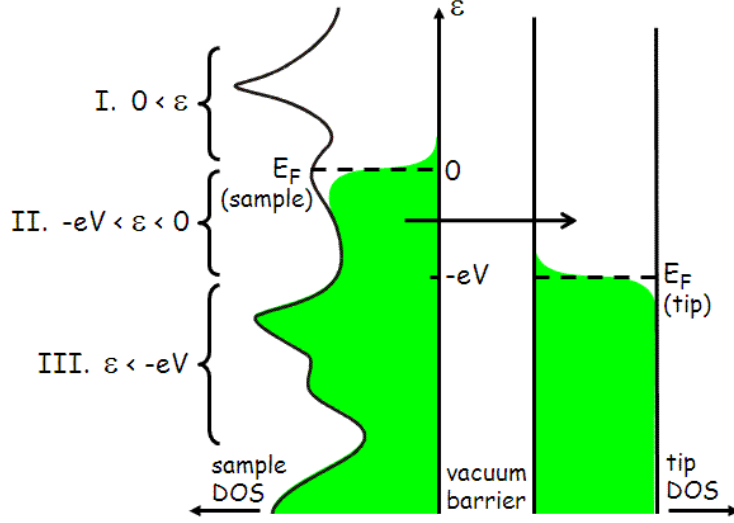


**Figure 7:** The density of states of both sample and tip after a (negative) voltage bias has been applied between sample and tip. In part I, no tunneling occurs because there are no filled states on either side. In part II, there are filled states in the sample and unfilled states in the tip, here a tunneling current can flow as indicated by the arrow. In part III, no tunneling current can flow because all states are filled. Source: <http://hoffman.physics.harvard.edu>

the determination of the current as

$$I \propto \sum_{\nu} |\psi_{\nu}(r_0)|^2 \delta(E_{\nu} - E_F) \quad (18)$$

where the sum is over the states  $\nu$  of the sample surface. By definition the LDOS is given by

$$\rho_{\nu}(r_0, E_F) \equiv \sum_{\nu} |\psi_{\nu}(r_0)|^2 \delta(E_{\nu} - E_F) \quad (19)$$

and thus the current is given by the LDOS beneath the centre of the tip. For a tip with radius of curvature of  $9\text{\AA}$ , excellent agreement was found with earlier measurements of Binnig *et al.* [55, 56]. It should be noted that in reality, the tunneling current can also have contributions from other states. In an extreme case, such as the case of graphite, this can lead to unrealistic predictions [57].

### 3.1.3 Operation principle of an STM

Now that we have discussed the theory of the STM, it is possible to discuss how a STM is operated in practice. As has been mentioned before, for the operation of an STM, a sharp metallic tip is brought close to the sample. Without a bias being applied, the system would simply equilibrate and no net current would flow. However, the situation changes when a bias voltage is applied from tip to sample or vice versa, see figure 7. Now, a current will start to flow, which was shown to be proportional to the surface LDOS measured at the centre of the tip according to the Tersoff-Hamann model, see equation (18).

In practice when operating the STM there are two modes of operation, the constant current mode and the constant height mode. When operating an STM in constant current mode, a feedback loop is used to keep the tunneling current constant. The current is kept constant by varying the tip-sample distance. By referring to equation (18), it is clear that what is measured in this mode is a contour of constant LDOS. In constant current mode it is important to operate using appropriate feedback loop parameters. Scanning using inappropriate settings results in oscillations or suboptimal resolution ('blurred' images). In a sense, the constant current mode is a safe operation mode in that the feedback loop avoids a tip crash on uneven sample surfaces.

In contrast, the constant height mode does not change the tip height and thus no feedback loop is required. In this mode, the tunneling current varies. The constant height mode is usually a faster way of obtaining an image because there is no time required for the feedback loop to operate. However, this does come at the disadvantage of a possible tip crash due to an uneven sample surface or drift.

## 3.2 Scanning tunneling spectroscopy

A related technique to STM is scanning tunneling spectroscopy (STS). Rather than taking an image of the surface at some constant voltage, the tip is held at a fixed position and the voltage is varied. In this way, the

$I - V$  characteristic of a location below the tip can be measured. In the following way, the surface LDOS beneath the tip can be extracted from the  $I - V$  characteristic: First, we refer to equation (17) for an expression of the current. For simplicity a constant tunneling matrix element is assumed and:

$$I \propto \int_0^{eV} \rho_S(E_F - eV + \epsilon) \rho_T(E_F + \epsilon) d\epsilon. \quad (20)$$

Since the tip is a metal and it can be assumed to have a flat DOS, in that case:

$$\frac{dI}{dV} \propto \rho_S(E_F - eV), \quad (21)$$

which means that  $dI/dV$  is proportional to the LDOS of the sample beneath the tip.

A problem with measuring the differential conductivity ( $dI/dV$ ) is that the tunneling current scales exponentially with both voltage and tip-sample separation [58]. To get rid of this dependency, a common normalization scheme is to divide by  $I/V$  proposed by Feenstra *et al.* [58]. See for instance the work of Lang for a discussion [59]. In this work, we will divide the differential conductivity by  $I/V$  to normalize the STS data.

In theory it is possible to measure the  $I-V$  characteristic of the sample and to then differentiate numerically. However, this will lead to a noisy measurement. Instead, it is common to use a lock-in amplifier. Here, the bias voltage of the STM ( $V_0$ ) is modulated with a small AC voltage  $V_{mod} = V_m \sin(\omega t)$ . We can find the response of the system using a Taylor expansion:

$$I(V) = I(V_0 + V_m \sin(\omega t)) = I(V_0) + \frac{dI}{dV} \sin(\omega t). \quad (22)$$

The lock-in amplifier picks the response at the driving frequency  $\omega$  which is the differential conductivity.

### 3.3 The experimental setup

All experiments in this thesis were carried out using the STM setup (Oxford Instruments Omicron Nanoscience) in figure 8. The system consists of two chambers, one for preparation of samples (yellow box in the figure) and

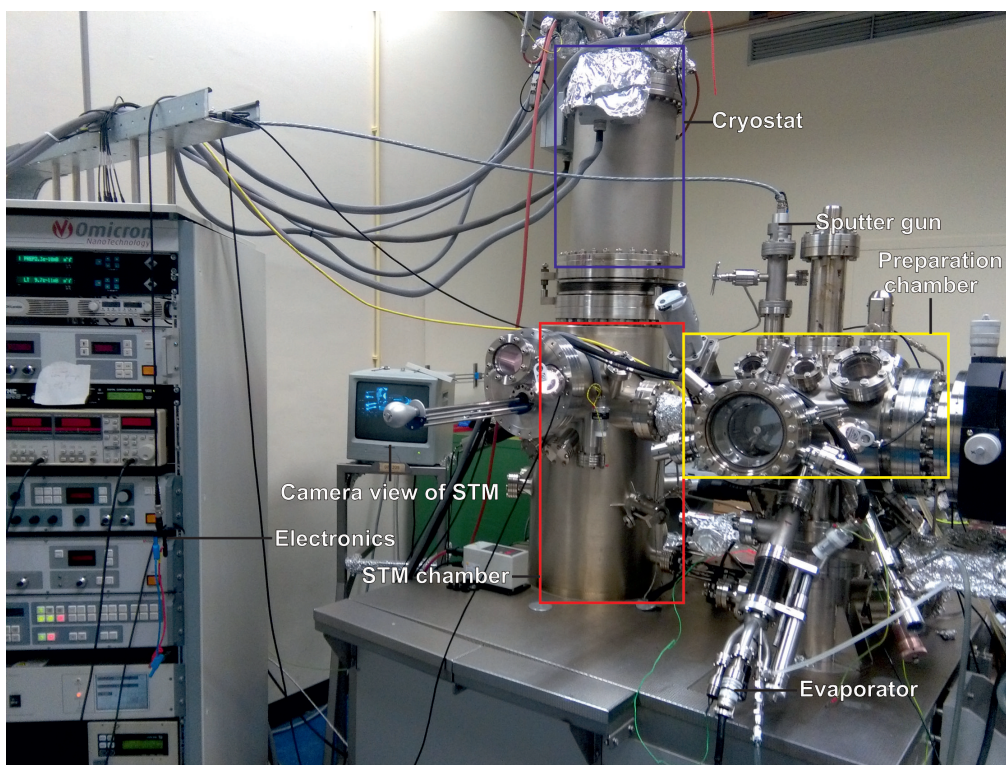


**Figure 8:** A photograph of the setup used for the experiments. The preparation chamber, STM chamber and cryostat are highlighted in the yellow, red and blue boxes respectively. The screen on the left of the table allows for viewing inside the STM chamber. On the bottom right, the evaporator used to deposit molecules on the sample is shown. On the left a rack with controls (labeled 'electronics' in the image) is visible which holds the controllers for the pumps, sputter gun (on top of the preparation chamber) and more.

one for sample storage and measurement (red box in the figure). The STM is suspended on springs inside the chamber and is equipped with Eddy current damping. Both chambers are continuously pumped to maintain an ultra high vacuum (UHV) environment (base pressure  $\approx 5 \times 10^{-10}$  mbar). The chambers are pumped by both ion and turbomolecular pumps, hidden underneath the table. In addition, underneath the table an active damping system can be found to remove low frequency noise. Furthermore, the system is equipped with a manipulator with resistive- and  $e^-$ -beam heating,  $\text{Ar}^+$  ion sputter gun, molecule evaporator and so forth. On top of the STM chamber is a cryostat (blue box in the figure) that can be filled with either liquid nitrogen ( $\text{LN}_2$ ) or liquid helium (LHe) to cool the STM.

### 3.4 Sample cleaning and preparation

This section serves a two-fold purpose. One is to describe the general cleaning procedure used to obtain clean single crystals<sup>3</sup>. The other is to describe the process of sample creation for this thesis.

Cleaning and general preparation of the single crystals is done by repeated cycles of  $\text{Ar}^+$  sputtering and annealing through resistive heating. The working of this process is two-fold. On a 'clean' single crystal (i.e. a single crystal with no molecules) the repeated cycles serve to create large atomically flat planes ('terraces'). For a single crystal covered with molecules, the cycles remove molecules to recover a clean single crystal.

To create the samples used for this thesis, 6,12-dibromochrysene (DBCh, see figure 9a), was deposited on a Au(111) single crystal, using the evaporator shown in figure 8. Note that DBCh is prochiral<sup>4</sup> in the gas phase and when it adsorbs on the surface it adsorbs either left- or right-handed. In the figure, both DBCh enantiomers are shown. To control the coverage of the molecules, a quartz crystal microbalance (QMB)<sup>5</sup> was used. Once

---

<sup>3</sup>A single crystal is a crystal where the periodic lattice is continuous up to the boundaries of the crystal. This means that it does not comprise different grains (as one would expect with any ordinary crystal) and rather consists of one large 'grain'.

<sup>4</sup>This means that DBCh can be converted to chiral in a single step, in this case it is made chiral by adsorbing onto the surface.

<sup>5</sup>A QMB is a quartz crystal (a piezoelectric) that is driven with a current at its

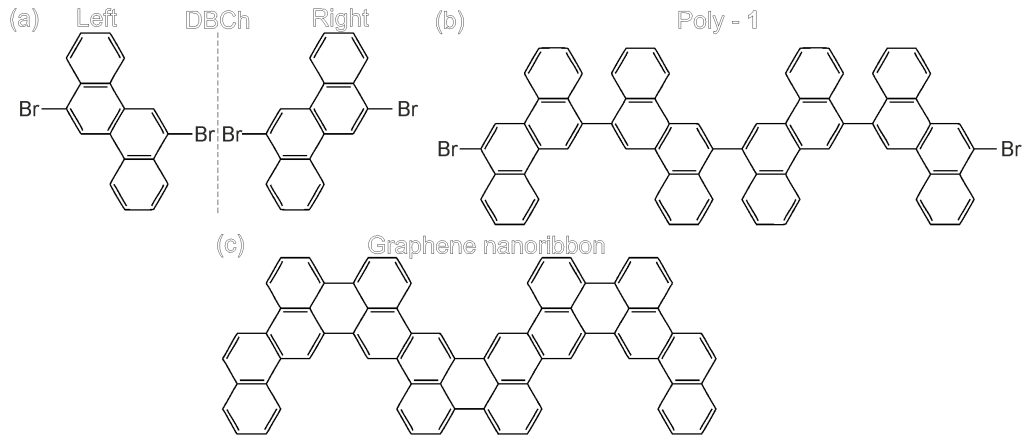


**Figure 9:** The three different stages of sample preparation: a) The prochiral DBCh molecule (both on-surface chiralities are given) b) The polymer which is formed after annealing to moderate temperatures. The polymer is formed by cleavage of bromine atoms from DBCh molecules and subsequent coupling of the dehalogenated molecules. c) The graphene nanoribbon obtained after a second annealing step. The ribbon is formed after the cyclodehydrogenation of poly-1. Both poly-1 and the GNR are truncated at 4 monomer units.

molecules were deposited, the sample could either be measured with the STM as-is or alternatively an annealing step could be performed. Annealing at moderate temperatures induced an Ullmann-type reaction between the DBCh molecules. The bromine atoms were first cleaved and subsequently a coupling of the dehalogenated molecules took place. The product of this reaction is the polymer, poly-1, which is shown in figure 9b. Annealing at higher temperatures caused cyclodehydrogenation, where two hydrogen atoms are cleaved from the polymer and an extra carbon-carbon bond was formed. The product of this reaction is the chevron-like GNR in figure 9c. Note that both the polymers and the GNRs are formed by alternating left- and right-handed DBCh enantiomers and are achiral.

---

resonance frequency. This current will cause the crystal to vibrate. When molecules are adsorbed onto the crystal, the amplitude of the vibrations induced by the current drops slightly. This is used as a very sensitive sorption detector, see [60].

## 4 Results

### 4.1 Self-assembled networks formed by DBCh on Au(111)

After deposition of DBCh (figure 9a) on Au(111), a long-range ordered porous self-assembled network formed (figure 10a). A single pore is formed by six left-handed or six right-handed DBCh enantiomers (figure 10d). The domains of the network are thus homochiral. Underneath the porous network, the Au(111) herringbone reconstruction is still visible, which indicates that the molecule-substrate interaction is weak [61]. In addition to the large domain (grey in figure 10a), a smaller domain (yellow in figure 10) formed. The angle between these two domains is approximately  $32^\circ$  in good agreement with previous results of Pham *et al* [13]. In between the two domains we obtain a noisy image, possibly due to mobile molecules.

The close-up image (figure 10b) reveals that the pores have a distinct curling star shape. Again, the larger domain is colored in grey whereas the smaller one is colored in yellow. Now it is important to note that DBCh is a prochiral molecule and adsorbs on the surface either left- or right-handed (see figure 9a). Upon closer inspection of the domains in figure 10b, it becomes clear that the pores in the majority and minority domains curl clockwise and counter-clockwise respectively. The change from clockwise to counter-clockwise curl cannot be achieved by a simple rotation. Thus the two domains are identified as being formed by enantiomers of opposite chirality and the domains are each others' mirror images. The tentative molecular model is given in figure 10c together with the unit cell. The structure features three-fold nodes where halogen bonding occurs, which stabilizes the network. The unit cell parameters of the porous network are as follows:  $a = b = 2.1 \pm 0.1$  nm and  $\alpha = 58^\circ \pm 3^\circ$ , forming a rhombic unit cell. We used STM images for the unit cell angle determination which can slightly distort angles due to thermal drift.

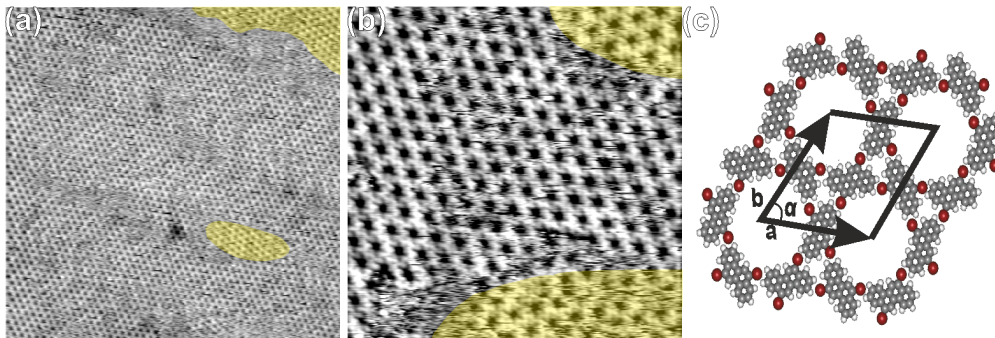


**Figure 10:** DBCh upon deposition of Au(111). a) An overview STM image ( $100 \times 100 \text{ nm}^2$ ) showing the long-range order of the porous network. The highlighted yellow areas show the different mirror domains (bias =  $-1.1 \text{ V}$ , setpoint =  $15 \text{ pA}$ ). b) A close-up STM image ( $30 \times 30 \text{ nm}^2$ ) of the porous network, revealing the star-shaped pores. The two mirror domains are shown in grey and yellow (bias =  $-1.1 \text{ V}$ , setpoint =  $15 \text{ pA}$ ). c) The tentative model in agreement with Pham *et al.* [13]. Colourcode: carbon: grey, hydrogen: white, bromine: red.

## 4.2 Chevron-like graphene nanoribbons from DBCh

Upon annealing samples with submonolayer coverage to  $155^\circ\text{C}$ , the DBCh molecules form graphene nanoribbons (figure 11a). The Au(111) reconstruction remains intact, once more indicating a weak interaction with the substrate [61]. Interestingly, the GNRs prefer to lie on the fcc regions of Au(111), indicating that the surface-molecule interaction is more energy favourable there. *A priori* one might expect one of two couplings to form the GNR: enantiomers mixed (LR) or enantiomers separated (LL) (see figure 9a). The straight sections of the GNR have a clear chevron shape and each 'elbow' of the chevron is identified as a perylene-like groups (see the molecular overlay on figure 11b). The chevron shape of the GNR indicates that the coupling took place in a LR fashion. The measured unit cell length is  $1.37 \pm 0.05 \text{ nm}$ , in agreement with the calculated length of  $1.34 \text{ nm}$ . Note that the chiral monomers coupled to form an achiral GNR. Thus the chirality from the monomers was not transferred to the GNR.

In figures 11a and b, in addition to straight segments, junctions are observed. These junctions appear to be caused by a secondary reaction, where the coupling does not occur on the bromine sites but rather on one of the exterior hydrogen atoms of the DBCh molecule (see figure 11c) causing

a cross-linking of two or more ribbons. The amount of cross-linking seems to depend on both the annealing temperature and annealing time, where higher temperature and longer time tends to cause more cross-linking.

In addition, occasionally sets of two bright spots were observed on some GNRs (see figure 12a). It becomes clear from the figure that the two bright spots are attached to a group approximately one-and-a-half times as long as a normal ribbon unit ( $\ell$  being the length of a normal unit in the figure). In addition, the two bright spots always appear at the same position with respect to each other, making impurities an unlikely cause. Instead, the two bright spots can be attributed to a coupling defect where instead of the regular LR (see figure 9a) coupling a single LL (or RR) coupling occurred (figure 12b). This coupling causes a steric repulsion between the hydrogen atoms encircled by the red ellipses in the figure. To accommodate for this, two aryl groups are tilted away from the surface (aryl 3 and 4 in the figure), which causes them to appear brighter in the image. Interestingly, at higher annealing temperatures a related defect was observed where the two protruding aryl groups became flat, i.e. they now lie on the same plane as the ribbon (see figure 12a, inset). In our proposed model, this could be caused by a further dehydrogenation of the ribbon and coupling at the hydrogen sites, forming two five-membered carbon rings.

On occasion, small entities appeared on the elbows of the reconstruction (see figure 9a). A closer look at the entities revealed that they come in six different varieties (figure 13a-f, top). The entities are all identified as dimers with either LR or LL coupling and varying amounts of bromine atoms attached. The tentative molecular model of each dimer is given in figure 13a-f, bottom. The origin of these dimers remains unknown, however the formation seems to be related to the deposition rate and annealing temperature where higher rates and temperatures tend to form less dimers. A reaction process where the DBCh enantiomers first dimerize and then couple to form the ribbons is unlikely, because we observed ribbons consisting of an odd number of monomers. Therefore, the dimers taking on the role of an intermediate reaction product is unlikely.

Lastly, we observed that when the sample was left at room temperature

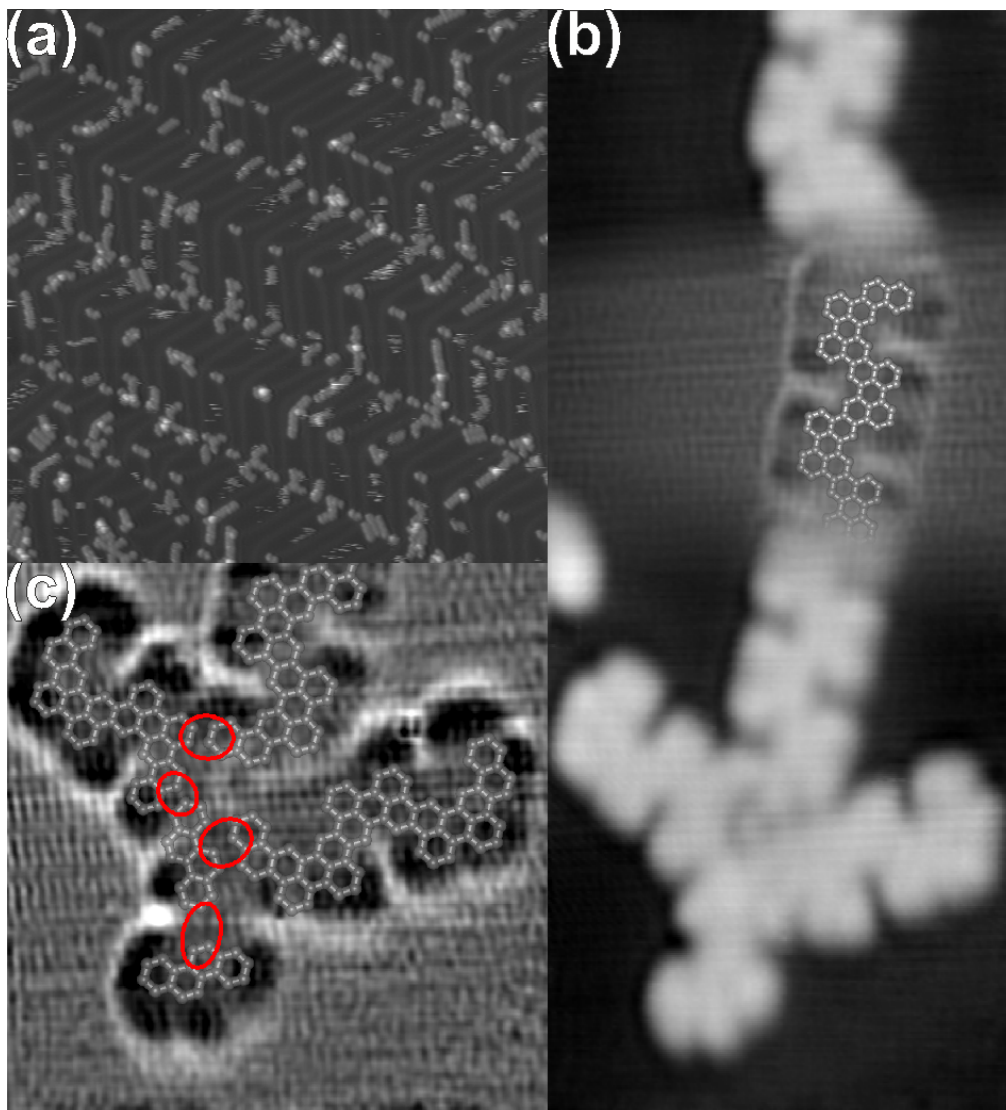


**Figure 11:** Chevron-like GNRs formed after annealing to 155 °C. a) A 100x100 nm<sup>2</sup> overview STM image of the sample (bias = -1.8V, setpoint = 5pA ). b) A close-up STM image (5.1x12 nm<sup>2</sup>) of a single GNR with its corresponding molecular model. To highlight the edges a Laplacian filter was partially overlaid (dark region). The lower half of the image displays cross-linking of three chains (bias = -1.8V, setpoint = 5pA). c) A Laplacian-filtered STM image of the lower section of the GNR from (b) with the overlaid molecular model for the cross-linking. Colorcode for the molecular model: carbon, grey. The exterior hydrogen atoms were omitted from the model for clarity.

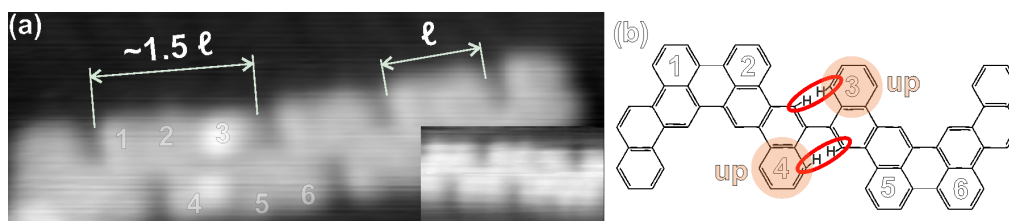


**Figure 12:** a) STM image showing two bright protrusions on a GNR ( $7.3 \times 2.6 \text{ nm}^2$ , bias =  $-2\text{V}$ , setpoint =  $5\text{pA}$ ). The increased length with respect to a normal perylene unit is also shown. The inset shows an STM image ( $4.2 \times 2.3 \text{ nm}^2$ , bias =  $-1.8\text{V}$ , setpoint =  $5\text{pA}$ ) of a related defect where further dehydrogenation took place and flattened the defect, bias = b) The proposed model of the stacking defect. The hydrogen atoms marked by red ellipses cause steric repulsion resulting in aryl groups 3 and 4 moving upward. The numbering of aryl groups in (a) corresponds to the numbering in (b).

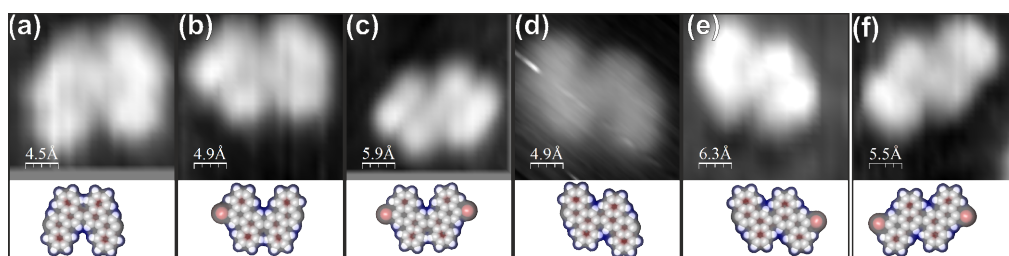


**Figure 13:** a-f) STM images showing the six different dimers observed together with their corresponding molecular model. For each molecular model, the van der Waals surface is also depicted. Colourcode: carbon: grey, hydrogen: white, bromine: red. Tunneling parameters (a-f): bias =  $-2\text{V}$ , setpoint =  $5\text{pA}$ .

for a prolonged period of time (a few days) the GNRs started to form aggregates as can be seen in figure 14a. A close-up STM image of one such structure (figure 14b) reveals that there has to be something between the GNRs, holding them together. When taking a closer look at the figure, dots are visible between the ribbons (some of which are highlighted in red). The dots can be either gold adatoms which diffused from the step edges or bromine atoms left on the surface after the initial Ullmann-type coupling reaction. Note that the temperature required for the initial Ullmann-type coupling is significantly lower than the required temperature for bromine atom desorption [62, 63]. Additionally, previous studies show that electronegative elements (such as bromine) can alter or lift the herringbone reconstruction [61, 64, 65]. In our case we observed that the reconstruction avoided the aggregates. Furthermore, in previous studies found that bromine atoms can form  $\text{Br} \cdots \text{H}$  bonds which aggregate molecules into close-packed structures [66–69]. Therefore, we attribute the dots to bromine atoms (some highlighted in the figure) which have formed  $\text{Br} \cdots \text{H}$  bonds with the ribbons, forming aggregates.

In addition to the structural analysis as described above, the electronic properties of the chevron GNR were investigated using STS. To probe the quality and cleanliness of the tip, an STS spectrum was taken of the bare Au(111) surface before and after each measurement. The Au(111) crystal has a surface state<sup>6</sup> at approximately -0.5 eV [70]. Thus, by probing the surface state of Au(111) before and after each measurement it is possible to assess the quality of the tip and allow for comparison of the surface's and GNRs' electronic properties, in particular their LDOS. The results of our STS measurements are summarized in figure 15. To achieve this figure, multiple STS measurements were performed in the middle of a GNR, far away from edges, bends and defects. Subsequently, the STS measurements were averaged. For clarity we have divided the  $dI/dV$  spectrum of the GNR by the spectrum surface, which accentuates their differences. The original

---

<sup>6</sup>Inside the metal bulk the electrons experience a periodic potential which abruptly changes to a hard wall potential at the surface. This abrupt change result in the presence of states located at the metal surface, known as surface states.

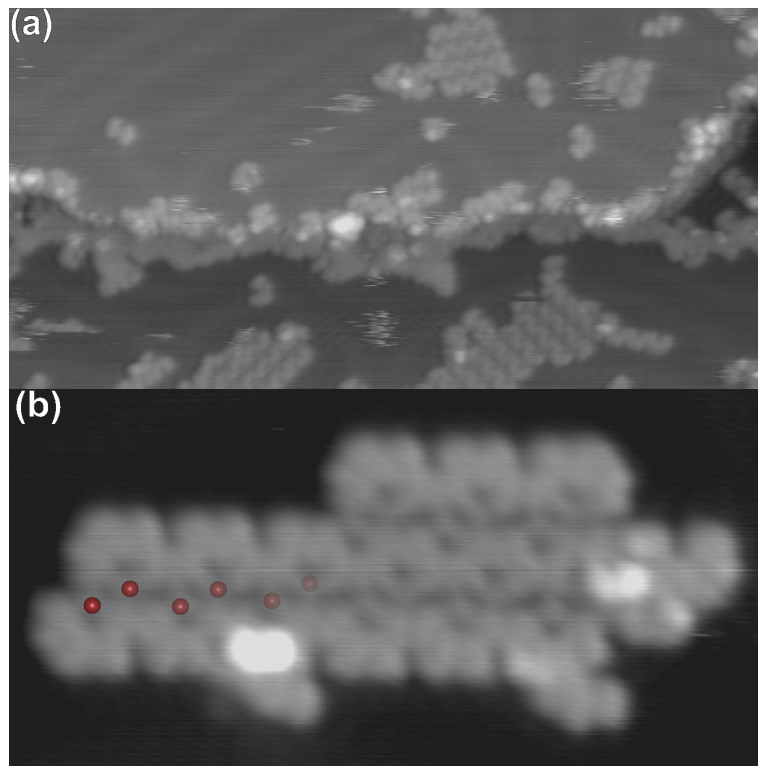


**Figure 14:** a) Overview STM image ( $50 \times 25 \text{ nm}^2$ ) of a sample where significant agglomeration took place (bias =  $-1.8 \text{ V}$ , setpoint =  $5 \text{ pA}$ ). b) A close-up STM image ( $11.6 \times 6.1 \text{ nm}^2$ ) of one such aggregate. In between the individual GNRs, small dots are visible. These are attributed to bromine atoms (red) left on the surface after Ullmann-type coupling (bias =  $-2 \text{ V}$ , setpoint =  $5 \text{ pA}$ ).

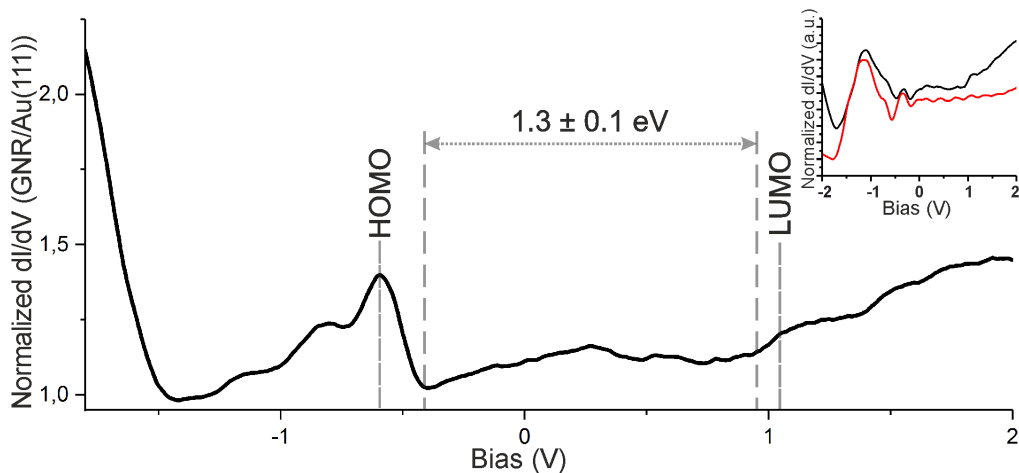


**Figure 15:** The differential conductance ( $dI/dV$ ) of a GNR divided by the differential conductance of the surface. Two states are identified within the spectrum, HOMO and LUMO respectively. The HOMO-LUMO gap is determined to be  $1.3 \pm 0.1$  eV. In the inset the measured  $dI/dV$  curves of Au(111) (red) and the GNR (black) are shown.

spectra are shown in the inset. Two peaks are labeled in figure 15, which are identified as the highest occupied molecular orbital (HOMO) and lowest unoccupied molecular orbital (LUMO<sup>7</sup>), respectively. The HOMO-LUMO gap, the difference in energy between the highest filled state and the lowest unfilled state is measured to be  $1.3 \pm 0.1$  eV. Thus, a substantial band gap is opened. The band gap we measured is in reasonable agreement with our gas-phase DFT calculations which resulted in a band gap of 1.05 eV. It is well known that DFT calculations using the local density approximation (LDA) for the exchange-correlation energy (as we did) tend to underestimate the band gap [71, 72]. At this point, it is interesting to note that the chevron-like GNR as synthesized in this thesis can be interpreted as a staggered version of the five wide armchair edge GNR (5-AGNR) previously synthesized by Zhang *et al.* [73]. The 5-AGNR is the smallest GNR in the  $3p + 2$ , narrow gap, family (see figure 5). Interestingly, Zhang *et al.* found a bandgap of  $2.8 \pm 0.1$  eV, much wider than *ab initio* calculations predict. Nevertheless, it is clear that the chevron-like GNR reported here

<sup>7</sup>The HOMO and LUMO, roughly speaking, are for molecules what the valence- and conduction band edges are for solids. In this analogy, the HOMO-LUMO gap takes on the role of the band gap.

has a substantially different band gap and is not the continuation of the 5-AGNR. Moreover, we can compare our chevron-like GNR to an AGNR with the same width, the 8-AGNR. Our DFT calculations yield a band gap of 1.05 eV for the chevron-like GNR, whereas the calculations of Son *et al.* (see figure 5) yield a band gap of approximately 0.25 eV. In addition, recently 8-AGNRs were synthesized on Au(111) single crystals by Sun *et al.*. Their characterization of the ribbons yielded a band gap of  $1.0 \pm 0.1$  eV [74]. Note that *GW* calculation of Yang *et al.* previously found a band gap of approximately 1.1 eV for the 8-AGNR [75]. Nevertheless, this result in combination with the comparison of the results of the DFT calculations, suggests it is likely that the band gap of our chevron-like GNR has increased with respect to an AGNR with the same width due to its chevron-like topology.

In addition to the  $dI/dV$  spectra, we performed differential conductance ( $dI/dV$ ) mapping<sup>8</sup> at various bias voltages:  $-2.0V$ ,  $-0.8V$  and  $1.5V$ . These voltages were chosen because of the peaks that were previously observed in the  $dI/dV$  spectra. This allows for an experimental observation of the spatial distribution of these states. The results are summarized in figure 16. From top to bottom each subfigure shows an STM topograph, a differential conductance map and a calculated LDOS map. As a visual guide the skeletal model of the GNR is overlaid on the same position on the ribbon in both the STM topograph and the differential conductance map. To obtain the differential conductance maps, the topographic image was extruded and the measured differential conductance was overlaid as a color scheme. In figure 16a, we see that the state at  $-2.0V$  sits mostly on the 'elbow' of the chevron-like GNR. The state at  $-2.0V$  is identified as the HOMO-2 and is in good agreement with the calculated LDOS map. The state at  $-0.8V$ , depicted in figure 16b, also appears mostly at the elbow however this state is, unlike the state at  $-2V$ , not uniformly distributed on the elbow. Lastly the state at  $1.5V$  (figure 16c) appears on both the elbow

---

<sup>8</sup>A differential conductance map shows the contribution of states close to a single bias voltage, unlike a regular STM image which shows contributions of all states between the bias voltage and the Fermi energy.

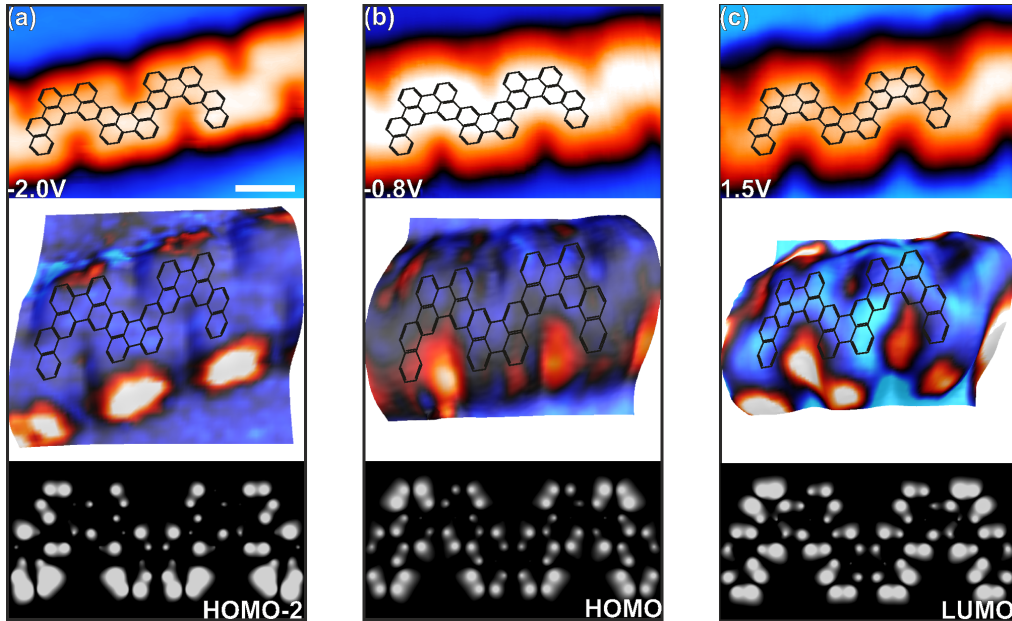


**Figure 16:** Differential conductance maps taken at a) -2V, b) -0.8V and c) 1.5V. From top to bottom each subfigure shows an STM topograph, a differential conductance map and a calculated LDOS map. Scale bar: 1 nm. The scale is the same for all STM topographs.

and inside the bay-like area of the chevron-like GNR. Note that  $-0.8\text{V}$  and  $1.5\text{V}$  at the boundary of two peaks in figure 15. Therefore it is possible that the tail of neighbouring states has influenced the differential conductance mapping. Nevertheless, the differential conductance maps for  $-0.8\text{V}$  and  $1.5\text{V}$  match our calculated LDOS maps for the HOMO and LUMO (respectively) reasonably well. Note that the distribution over the sides to the ribbon is uneven in all cases, for both the measurement data and the calculated LDOS maps. Interestingly, these states all have increased density close to the edges of the chevron-like GNR as is apparent from both the measured and calculated differential conductance maps. Similar results were previously reported by other authors [16, 17, 76]. These ribbons all have armchair edges, similar to ours, but are much wider at 15 to 19 carbon atoms width.

## 5 Discussion

The goal of this study was to synthesize chevron-like GNRs from molecular precursors and to probe their structural and electronic properties. In this study we found that DBCh when deposited at room temperature formed a long-range ordered porous network on Au(111) stabilized by three-fold halogen bonding nodes. Similar to previous studies [23, 77, 78] DBCh self-assembled in homochiral networks. Upon annealing of the sample at 155 °C, in addition to the chevron-like GNRs, we observed small molecular species which we identified as dimers. The cause for the formation of the dimers remains unknown, however it seems to be related to the annealing temperature, where a lower temperature increases the amount of dimers. The dimers being an intermediate reaction product is unlikely, because we observe ribbons consisting of an odd amount of monomers.

The main result of this study is the characterization of the electronic properties of the chevron-like GNRs. Using STS, it was found that the GNRs are semiconducting with a band gap of  $1.3 \pm 0.1$  eV. Although structurally the GNR might appear as the staggered version of the 5-AGNR, it has a significantly smaller band gap. The AGNR with the same width as the chevron-like GNR was reported to have a band gap of  $1.0 \pm 0.1$  eV [74]. Similarly, our DFT calculations resulted in a band gap of 1.05 eV for our chevron-like GNR. Similar DFT calculations for the 8-AGNR by Son *et al.* yielded a band gap of approximately 0.25 eV. Thus, it appears that the band gap of the chevron-like GNR is larger than that of an AGNR of the same width.

Our differential conductance maps were taken at 77K, whereas most other studies were done at approximately 4K. Because of the long time it takes to obtain one differential conductance map, one might expect that thermal drift would elongate/shorten the features of the GNRs and thus influence the differential conductance maps. However, the change in length and width of the ribbons in the STM images is only moderate. The increased density of states at certain locations on the edges of the ribbon (either the bay-like area or on the elbow of the chevron), i.e. the edge states, is similar to results of previous authors who studied wider armchair

GNRs (between 15 and 19 carbon atoms wide) [16, 17, 76].

## 6 Conclusion

In conclusion, we synthesized chevron-like GNRs on Au(111) from a prochiral precursor (6,12,-dibromochrysene). The objective of this study was to characterize the electronic properties of this GNR. We measured the band gap of the chevron-like GNRs to be  $1.3 \pm 0.1$  eV, which is in agreement with our gas-phase DFT calculations. In addition, we found that the states of the chevron-like GNRs appear mostly on the edges, both in our experimental differential conductance mapping and our calculated LDOS maps. This type of distribution was previously observed in other chevron GNRs [16, 17, 76]. It is likely that the band gap of the chevron-like GNR widened with respect to an AGNR of the same width due to its chevron shape. This opens up new possibilities to further tune the band gap of GNRs by considering GNRs of shapes other than armchair and zigzag.

## References

- <sup>1</sup>G. E. Moore, *Electronics* **38**, 114–117 (1965).
- <sup>2</sup>J. Cai, P. Ruffieux, R. Jaafar, M. Bieri, T. Braun, S. Blankenburg, M. Muoth, A. P. Seitsonen, M. Saleh, X. Feng, K. Müllen, and R. Fasel, *Nature* **466**, 470–473 (2010).
- <sup>3</sup>K. S. Novoselov, A. K. Geim, S. V. Morozov, D. Jiang, Y. Zhang, S. V. Dubonos, I. V. Grigorieva, and A. A. Firsov, *Science* **306**, 666–669 (2004).
- <sup>4</sup>K. I. Bolotin, K. J. Sikes, Z. Jiang, M. Klima, G. Fudenberg, J. Hone, P. Kim, and H. L. Stormer, *Solid State Communications* **146**, arXiv: 0802.2389, 351–355 (2008).
- <sup>5</sup>X. Zhang, O. V. Yazyev, J. Feng, L. Xie, C. Tao, Y.-C. Chen, L. Jiao, Z. Pedramrazi, A. Zettl, S. G. Louie, H. Dai, and M. F. Crommie, *ACS Nano* **7**, 198–202 (2013).
- <sup>6</sup>L. Ma, J. Wang, and F. Ding, *ChemPhysChem* **14**, 47–54 (2013).
- <sup>7</sup>L. Talirz, H. Söde, T. Dumslaff, S. Wang, J. R. Sanchez-Valencia, J. Liu, P. Shinde, C. A. Pignedoli, L. Liang, V. Meunier, N. C. Plumb, M. Shi, X. Feng, A. Narita, K. Müllen, R. Fasel, and P. Ruffieux, *ACS Nano* **11**, 1380–1388 (2017).
- <sup>8</sup>A. Kimouche, M. M. Ervasti, R. Drost, S. Halonen, A. Harju, P. M. Joensuu, J. Sainio, and P. Liljeroth, *Nature Communications* **6** (2015).
- <sup>9</sup>Y.-C. Chen, D. G. de Oteyza, Z. Pedramrazi, C. Chen, F. R. Fischer, and M. F. Crommie, *ACS Nano* **7**, 6123–6128 (2013).
- <sup>10</sup>P. Ruffieux, S. Wang, B. Yang, C. Sánchez-Sánchez, J. Liu, T. Dienel, L. Talirz, P. Shinde, C. A. Pignedoli, D. Passerone, T. Dumslaff, X. Feng, K. Müllen, and R. Fasel, *Nature* **531**, 489–492 (2016).
- <sup>11</sup>F. Schulz, P. H. Jacobse, F. F. Canova, J. van der Lit, D. Z. Gao, A. van den Hoogenband, P. Han, R. J. Klein Gebbink, M.-E. Moret, P. M. Joensuu, I. Swart, and P. Liljeroth, *The Journal of Physical Chemistry C* **121**, 2896–2904 (2017).

- <sup>12</sup>N. Merino-Díez, J. Li, A. Garcia-Lekue, G. Vasseur, M. Vilas-Varela, E. Carbonell-Sanromà, M. Corso, J. E. Ortega, D. Peña, J. I. Pascual, and D. G. de Oteyza, *The Journal of Physical Chemistry Letters* **9**, 25–30 (2018).
- <sup>13</sup>T. A. Pham, B. V. Tran, M.-T. Nguyen, and M. Stöhr, *Small* **13**, 1603675 (2017).
- <sup>14</sup>O. Gröning, S. Wang, X. Yao, C. A. Pignedoli, G. Borin Barin, C. Daniels, A. Cupo, V. Meunier, X. Feng, A. Narita, K. Müllen, P. Ruffieux, and R. Fasel, *Nature* **560**, 209–213 (2018).
- <sup>15</sup>J. Cai, C. A. Pignedoli, L. Talirz, P. Ruffieux, H. Söde, L. Liang, V. Meunier, R. Berger, R. Li, X. Feng, K. Müllen, and R. Fasel, *Nature Nanotechnology* **9**, 896–900 (2014).
- <sup>16</sup>G. D. Nguyen, H.-Z. Tsai, A. A. Omrani, T. Marangoni, M. Wu, D. J. Rizzo, G. F. Rodgers, R. R. Cloke, R. A. Durr, Y. Sakai, F. Liou, A. S. Aikawa, J. R. Chelikowsky, S. G. Louie, F. R. Fischer, and M. F. Crommie, *Nature Nanotechnology* **12**, 1077–1082 (2017).
- <sup>17</sup>C. Bronner, R. A. Durr, D. J. Rizzo, Y.-L. Lee, T. Marangoni, A. M. Kalayjian, H. Rodriguez, W. Zhao, S. G. Louie, F. R. Fischer, and M. F. Crommie, *ACS Nano* **12**, 2193–2200 (2018).
- <sup>18</sup>D. J. Rizzo, G. Veber, T. Cao, C. Bronner, T. Chen, F. Zhao, H. Rodriguez, S. G. Louie, M. F. Crommie, and F. R. Fischer, *Nature* **560**, 204–208 (2018).
- <sup>19</sup>Y.-C. Chen, T. Cao, C. Chen, Z. Pedramrazi, D. Haberer, D. G. de Oteyza, F. R. Fischer, S. G. Louie, and M. F. Crommie, *Nature Nanotechnology* **10**, 156–160 (2015).
- <sup>20</sup>S. Blankenburg, J. Cai, P. Ruffieux, R. Jaafar, D. Passerone, X. Feng, K. Müllen, R. Fasel, and C. A. Pignedoli, *ACS Nano* **6**, 2020–2025 (2012).
- <sup>21</sup>G. Binnig, H. Rohrer, C. Gerber, and E. Weibel, *Physical Review Letters* **50**, 120–123 (1983).
- <sup>22</sup>J.-M. Lehn, *Angewandte Chemie International Edition in English* **27**, 89–112 (1988).

- <sup>23</sup>J. A. Elemans, S. Lei, and S. De Feyter, *Angewandte Chemie International Edition* **48**, 7298–7332 (2009).
- <sup>24</sup>G. M. Whitesides, J. P. Mathias, and C. T. Seto, *Science* **254**, 1312–1319 (1991).
- <sup>25</sup>J. M. A. Carnall, C. A. Waudby, A. M. Belenguer, M. C. A. Stuart, J. J.-P. Peyralans, and S. Otto, *Science* **327**, 1502–1506 (2010).
- <sup>26</sup>M. Böhringer, K. Morgenstern, W.-D. Schneider, R. Berndt, F. Mauri, A. De Vita, and R. Car, *Physical Review Letters* **83**, 324–327 (1999).
- <sup>27</sup>G. Pawin, K. L. Wong, K.-Y. Kwon, and L. Bartels, *Science* **313**, 961–962 (2006).
- <sup>28</sup>A. Kühnle, *Current Opinion in Colloid & Interface Science* **14**, 157–168 (2009).
- <sup>29</sup>J. A. Theobald, N. S. Oxtoby, M. A. Phillips, N. R. Champness, and P. H. Beton, *Nature* **424**, 1029–1031 (2003).
- <sup>30</sup>M. E. Cañas-Ventura, W. Xiao, D. Wasserfallen, K. Müllen, H. Brune, J. V. Barth, and R. Fasel, *Angewandte Chemie International Edition* **46**, 1814–1818 (2007).
- <sup>31</sup>D. Payer, A. Comisso, A. Dmitriev, T. Strunskus, N. Lin, C. Wöll, A. DeVita, J. V. Barth, and K. Kern, *Chemistry – A European Journal* **13**, 3900–3906 (2007).
- <sup>32</sup>P. Politzer, J. S. Murray, and T. Clark, *Physical Chemistry Chemical Physics* **15**, 11178 (2013).
- <sup>33</sup>T. Brinck, J. S. Murray, and P. Politzer, *International Journal of Quantum Chemistry* **44**, 57–64 (1992).
- <sup>34</sup>A. Priimagi, G. Cavallo, P. Metrangolo, and G. Resnati, *Accounts of Chemical Research* **46**, 2686–2695 (2013).
- <sup>35</sup>B. Rogers, J. Adams, and S. Pennathur (CRC Press, 2011).
- <sup>36</sup>S. Furukawa, K. Tahara, F. C. De Schryver, M. Van der Auweraer, Y. Tobe, and S. De Feyter, *Angewandte Chemie International Edition* **46**, 2831–2834 (2007).

- <sup>37</sup>H.-Y. Gao, H. Wagner, P. A. Held, S. Du, H.-J. Gao, A. Studer, and H. Fuchs, *Applied Physics Letters* **106**, 081606 (2015).
- <sup>38</sup>N. Merino-Díez, J. Lobo-Checa, P. Nita, A. Garcia-Lekue, A. Basagni, G. Vasseur, F. Tiso, F. Sedona, P. K. Das, J. Fujii, I. Vobornik, M. Sambì, J. I. Pascual, J. E. Ortega, and D. G. de Oteyza, *The Journal of Physical Chemistry Letters* **9**, 2510–2517 (2018).
- <sup>39</sup>S. Lukas, G. Witte, and C. Wöll, *Physical Review Letters* **88**, 028301 (2001).
- <sup>40</sup>F. Ullmann and J. Bielecki, *Berichte der deutschen chemischen Gesellschaft* **34**, 2174–2185 (1901).
- <sup>41</sup>C. Sambì, S. P. Marsden, A. J. Blacker, and P. C. McGowan, *Chemical Society Reviews* **43**, 3525–3550 (2014).
- <sup>42</sup>M. Lackinger, *Chemical Communications* **53**, 7872–7885 (2017).
- <sup>43</sup>L. Grill, M. Dyer, L. Lafferentz, M. Persson, M. V. Peters, and S. Hecht, *Nature nanotechnology* **2**, 687 (2007).
- <sup>44</sup>D. G. de Oteyza, A. García-Lekue, M. Vilas-Varela, N. Merino-Díez, E. Carbonell-Sanromà, M. Corso, G. Vasseur, C. Rogero, E. Guitián, J. I. Pascual, J. E. Ortega, Y. Wakayama, and D. Peña, *ACS Nano* **10**, 9000–9008 (2016).
- <sup>45</sup>M. Treier, C. A. Pignedoli, T. Laino, R. Rieger, K. Müllen, D. Passerone, and R. Fasel, *Nature Chemistry* **3**, 61–67 (2011).
- <sup>46</sup>A. H. Castro Neto, F. Guinea, N. M. R. Peres, K. S. Novoselov, and A. K. Geim, *Reviews of Modern Physics* **81**, 109–162 (2009).
- <sup>47</sup>A. K. Geim and K. S. Novoselov, *Nature Materials* **6**, 183–191 (2007).
- <sup>48</sup>K. Nakada, M. Fujita, G. Dresselhaus, and M. S. Dresselhaus, *Physical Review B* **54**, 17954–17961 (1996).
- <sup>49</sup>Y.-W. Son, M. L. Cohen, and S. G. Louie, *Physical Review Letters* **97** (2006).
- <sup>50</sup>G. Binnig, H. Rohrer, C. Gerber, and E. Weibel, *Applied Physics Letters* **40**, 178–180 (1982).

- <sup>51</sup>F. S. Levin (Cambridge University Press, 2002).
- <sup>52</sup>C. J. Chen (Oxford University Press on Demand, 1993).
- <sup>53</sup>V. V. Mitin, D. I. Sementsov, and N. Z. Vagidov (Cambridge University Press, 2010).
- <sup>54</sup>J. Bardeen, *Physical Review Letters* **6**, 57–59 (1961).
- <sup>55</sup>J. Tersoff and D. R. Hamann, *Physical Review B* **31**, 805–813 (1985).
- <sup>56</sup>G. Binnig, H. Rohrer, C. Gerber, and E. Weibel, *Surface Science* **131**, 379–384 (1983).
- <sup>57</sup>J. Tersoff and N. D. Lang, *Physical Review Letters* **65**, 1132–1135 (1990).
- <sup>58</sup>J. A. Stroscio, R. M. Feenstra, and A. P. Fein, *Physical Review Letters* **57**, 2579–2582 (1986).
- <sup>59</sup>N. D. Lang, *Physical Review B* **34**, 5947–5950 (1986).
- <sup>60</sup>W. H. King, *Analytical Chemistry* **36**, 1735–1739 (1964).
- <sup>61</sup>E. V. Iski, A. D. Jewell, H. L. Tierney, G. Kyriakou, and E. C. H. Sykes, *Journal of Vacuum Science & Technology A: Vacuum, Surfaces, and Films* **29**, 040601 (2011).
- <sup>62</sup>J. Björk, F. Hanke, and S. Stafström, *Journal of the American Chemical Society* **135**, 5768–5775 (2013).
- <sup>63</sup>C. Bronner, J. Björk, and P. Tegeder, *The Journal of Physical Chemistry C* **119**, 486–493 (2015).
- <sup>64</sup>A. Saywell, W. Greń, G. Franc, A. Gourdon, X. Bouju, and L. Grill, *The Journal of Physical Chemistry C* **118**, 1719–1728 (2014).
- <sup>65</sup>T. A. Pham, F. Song, M.-T. Nguyen, Z. Li, F. Studener, and M. Stöhr, *Chemistry – A European Journal* **22**, 5937–5944 (2016).
- <sup>66</sup>T. Wang, H. Lv, Q. Fan, L. Feng, X. Wu, and J. Zhu, *Angewandte Chemie International Edition* **56**, 4762–4766 (2017).
- <sup>67</sup>J. Dai, Q. Fan, T. Wang, J. Kuttner, G. Hilt, J. M. Gottfried, and J. Zhu, *Physical Chemistry Chemical Physics* **18**, 20627–20634 (2016).

- <sup>68</sup>T. Wang, J. Huang, H. Lv, Q. Fan, L. Feng, Z. Tao, H. Ju, X. Wu, S. L. Tait, and J. Zhu, *Journal of the American Chemical Society* **140**, 13421–13428 (2018).
- <sup>69</sup>J. A. Lipton-Duffin, O. Ivasenko, D. F. Perepichka, and F. Rosei, *Small* **5**, 592–597 (2009).
- <sup>70</sup>T. Andreev, I. Barke, and H. Hövel, *Physical Review B* **70** (2004).
- <sup>71</sup>J. P. Perdew and M. Levy, *Physical Review Letters* **51**, 1884–1887 (1983).
- <sup>72</sup>J. M. Crowley, J. Tahir-Kheli, and W. A. Goddard, *The Journal of Physical Chemistry Letters* **7**, 1198–1203 (2016).
- <sup>73</sup>H. Zhang, H. Lin, K. Sun, L. Chen, Y. Zagranyski, N. Aghdassi, S. Duhm, Q. Li, D. Zhong, Y. Li, K. Müllen, H. Fuchs, and L. Chi, *Journal of the American Chemical Society* **137**, 4022–4025 (2015).
- <sup>74</sup>K. Sun, P. Ji, J. Zhang, J. Wang, X. Li, X. Xu, H. Zhang, and L. Chi, *Small* **0**, 1804526 (2019).
- <sup>75</sup>L. Yang, C.-H. Park, Y.-W. Son, M. L. Cohen, and S. G. Louie, *Physical Review Letters* **99** (2007).
- <sup>76</sup>R. A. Durr, D. Haberer, Y.-L. Lee, R. Blackwell, A. M. Kalayjian, T. Marangoni, J. Ihm, S. G. Louie, and F. R. Fischer, *Journal of the American Chemical Society* **140**, 807–813 (2018).
- <sup>77</sup>S. Weigelt, C. Busse, L. Petersen, E. Rauls, B. Hammer, K. V. Gothelf, F. Besenbacher, and T. R. Linderoth, *Nature Materials* **5**, 112–117 (2006).
- <sup>78</sup>A. G. Slater, Y. Hu, L. Yang, S. P. Argent, W. Lewis, M. O. Blunt, and N. R. Champness, *Chemical Science* **6**, 1562–1569 (2015).

## 7 Acknowledgements

Science and research is a team effort and without the help and guidance of the members of the Surface Science group this thesis would have never been written. Therefore, I want to express my gratitude to all who have helped me during the past nine months.

First of all, I would like to thank prof. dr. Meike Stöhr for giving me this interesting and exciting project and for her guidance during this project. Dear Meike, I would like to thank you for the support you have given me. Discussions we had helped me gain a deeper understanding over the course of my research here. I would also like to thank you for trusting me to represent the group by letting me present our work at the DPG spring meeting, which has been a very exciting and educational experience for me. Lastly, I would like to thank you for giving me the opportunity to continue doing research in this group in the upcoming four years.

I would like to thank prof. dr. Tamalika Banerjee for agreeing to be my second examiner.

My special gratitude goes out to dr. Mihaela Enache, my daily supervisor, who has helped me tremendously during the course of the project. Dear Miki, the first few months you have taught me how to operate the machine. You have been a good teacher and you have always been patient with me. During the entire project, if I did not understand or was not sure about something I could always knock on your door and you would help me. For this, I am very thankful. I would also like to thank you for performing the DFT calculations, which have been very helpful for the project.

I would like to thank all the members of the Surface Science, Meike, Miki, Nico, Leonid, Brian, Ida, Wenbo and Joris not only for the work we have done together but also for the nice working environment and the fun time we had. In the same vein, I would like to thank the members of the Surfaces and Thin Films group, Petra, Oreste, Ali, Feng, Elini, Tashfeen, Theodosios, Estella and Pascal.

Lastly, I would like to thank dr. Tuan Anh Pham and dr. Van Bay Tran for laying the foundation of this project which I could build upon.